Deriving models for the Kitaev spin-liquid candidate material α-$RuCl_3$ from first principles

Casey Eichstaedt,[1,2] Yi Zhang,[3,4] Pontus Laurell,[5] Satoshi Okamoto,[6,*] Adolfo G. Eguiluz,[1,2,†] and Tom Berlijn[5,7,‡]

[1]*Department of Physics and Astronomy, University of Tennessee, Knoxville, Tennessee 37996, USA*
[2]*Joint Institute of Advanced Materials, University of Tennessee, Knoxville, Tennessee 37996, USA*
[3]*Department of Physics and Astronomy, Louisiana State University, Baton Rouge, Louisiana 70803, USA*
[4]*Center for Computation and Technology, Louisiana State University, Baton Rouge, Louisiana 70803, USA*
[5]*Center for Nanophase Materials Sciences, Oak Ridge National Laboratory, Oak Ridge, Tennessee 37831, USA*
[6]*Materials Science and Technology Division, Oak Ridge National Laboratory, Oak Ridge, Tennessee 37831, USA*
[7]*Computer Science and Mathematics Division, Oak Ridge National Laboratory, Oak Ridge, Tennessee 37831, USA*

(Received 2 April 2019; revised manuscript received 23 June 2019; published 6 August 2019)

We use the constrained random phase approximation to derive from first principles the Ru-t_{2g} Wannier-function-based model for the Kitaev spin-liquid candidate material α-$RuCl_3$. We find the nonlocal Coulomb repulsion to be sizable compared to the local one. In addition we obtain the contribution to the Hamiltonian from the spin-orbit coupling and find it to also contain non-negligible nonlocal terms. We invoke strong-coupling perturbation theory to investigate the influence of these nonlocal elements of the Coulomb repulsion and the spin-orbit coupling on the magnetic interactions. We find that the nonlocal Coulomb repulsions cause a strong enhancement of the magnetic interactions, which deviate from experimental fits reported in the literature. Our results contribute to the understanding and design of quantum spin-liquid materials via first-principles calculations.

DOI: 10.1103/PhysRevB.100.075110

I. INTRODUCTION

In his seminal paper, Kitaev presented an exact solution of the Kitaev model and found it to host a quantum spin-liquid ground state with fractionalized Majorana fermion and gauge flux excitations [1]. This exotic state of matter is not only interesting from a fundamental scientific point of view but also has been proposed to have potential applications in topological quantum computing [2,3]. Further progress was made by the idea that the Kitaev quantum spin liquid can possibly be realized in the materials family of the honeycomb iridates A_2IrO_3 with $A = \mathrm{Na}, \mathrm{Li}$ [4,5]. Assuming that in A_2IrO_3 the electrons are in the strong-coupling limit, in which the interactions dominate over the kinetic energy, and taking into account the spin-orbit coupling, oxidation state, and crystal field splitting in the Ir atoms, it was concluded that this compound contains strong Kitaev interactions, in addition to the usual Heisenberg exchange couplings. Depending on the materials parameters it was found that the system can be pushed from an antiferromagnetic (AFM) stripy state into the desired quantum spin-liquid state. However, based on combined theoretical and experimental findings it was deduced that A_2IrO_3 displays AFM zigzag order instead of the AFM stripy order or the quantum spin-liquid ground state [6]. This was later confirmed by other experiments [7,8]. To account for the experimentally observed zigzag state it was clear that an accurate description of A_2IrO_3 needed to involve extension beyond the Heisenberg-Kitaev model. To that end it was proposed that second and third nearest-neighbor Heisenberg exchange couplings can stabilize the experimentally observed AFM zigzag configuration [9]. Alternatively, first-principles simulations have shown that A_2IrO_3 contains strong nearest-neighbor magnetic anisotropic interactions that favor the AFM zigzag state [10]. In a third opposite picture it is assumed that A_2IrO_3 is not in the strong-coupling limit, but that instead the strong oxygen-assisted hopping between the Ir atoms causes the electrons to delocalize into quasimolecular orbitals [11].

Another closely related Kitaev spin-liquid candidate material is α-$RuCl_3$. The chemically active Ru transition metals in this compound form a honeycomb lattice with five d electrons per atom with strong spin-orbit coupling and electron-electron interactions in the presence of an octahedral crystal field induced by the Cl anions. Therefore, just like with A_2IrO_3, the materials specifics of α-$RuCl_3$ appear to fulfill the conditions laid out in Ref. [5] for the emergence of Kitaev interactions [12,13]. Inelastic-neutron-scattering experiments [14] on α-$RuCl_3$ displayed in addition to AFM zigzag order [14–17] a broad continuum in the magnetic excitation spectrum that is indicative of fractionalized excitations. This led to the conclusion that α-$RuCl_3$ is proximate to being in the desired quantum spin-liquid phase [14]. More recent neutron-scattering experiments have shown that the AFM zigzag order can be suppressed by applying an 8 T magnetic field yielding a magnetic excitation spectrum consistent with a quantum spin-liquid phase [18]. Further evidence for the quantum spin-liquid phase has been provided by the observation of the thermal quantum Hall effect in α-$RuCl_3$ at similar magnetic field strengths [19].

*okapon@ornl.gov
†eguiluz@utk.edu
‡tberlijn@gmail.com

In order to understand the properties of α-$RuCl_3$ and to investigate how this material can be manipulated towards potential applications in topological quantum computing, a microscopic understanding is essential. For that purpose there has been a large effort to map out the magnetic exchange couplings of α-$RuCl_3$ both via experimental and theoretical techniques [20–29]. On the experimental side, models have been derived by fitting a generalized spin model to various experiments such as inelastic neutron scattering [20,28], THz spectroscopy [21], anisotropic-susceptibility measurements [22], magnetic-specific-heat measurements [26,30,31], and thermal Hall effect measurements [32,33]. The derived magnetic interactions via these fits, however, display large variations depending on the experiments. In some of the purely theoretical approaches the magnetic interactions are derived by computing the hopping parameters of the Ru-t_{2g} electrons from first principles while their interaction parameters are taken to be some assumed values [13,23,25,29,34]. In another theoretical approach the first-neighboring magnetic interactions are derived from first principles via quantum chemistry techniques, while the second- and third-neighboring magnetic exchange couplings are modeled phenomenologically [24]. However, there has not been to the best of our knowledge an attempt to derive the magnetic model of α-$RuCl_3$ fully from first principles.

In this paper, we derive the spin model of α-$RuCl_3$ fully from first principles. To that end, we first employ density functional theory (DFT), the constrained random phase approximation (cRPA), and the projected Wannier function method to obtain a low-energy, generalized Hubbard Hamiltonian for a Hilbert space spanned by Ru-t_{2g} Wannier orbitals. In a second stage we apply second-order perturbation theory in the strong-coupling limit to our Hamiltonian and obtain the model with spin degrees of freedom only. We find that in the generalized Hubbard model the interatomic Coulomb repulsions and spin-orbit coupling effects are relatively strong compared to their intra-atomic counterparts. The effect of the interatomic interactions is found to strongly enhance the nearest-neighboring magnetic couplings by a factor 3–7. The effect of the interatomic spin-orbit effects is mainly to enhance the Kitaev coupling by 14%. The magnetic interactions in our first-principles spin model deviate significantly from the values obtained by fitting experiments. We discuss potential shortcomings in our theoretical approach. Our findings allow for a better understanding of α-$RuCl_3$ and quantum spin-liquid materials in general via first-principles calculations.

II. METHODS

In order to derive the spin model for α-$RuCl_3$ from first principles we perform the four-step procedure described in Fig. 1(a). Below we will briefly review the methodology behind each of the steps. More details about these methods can be found in Refs. [10,35–37].

The first step is to perform DFT calculations of α-$RuCl_3$ to obtain the Kohn-Sham eigenvalues and eigenfunctions. The DFT calculations were performed within the generalized gradient approximation using the Perdew-Burke-Ernzerhof exchange correlation scheme [38] and the linear augmented plane wave (LAPW) method as implemented in the ELK code

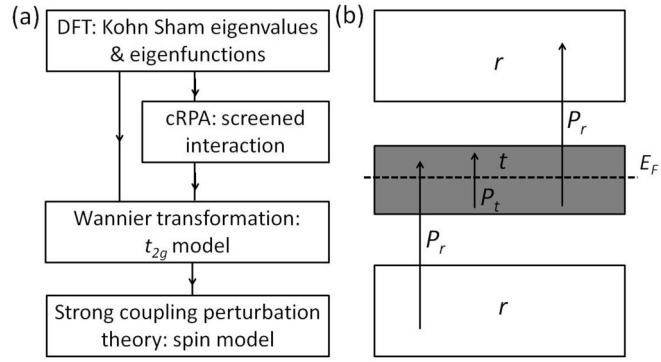

FIG. 1. (a) Flow diagram of methods used: density functional theory (DFT), constrained random phase approximation (cRPA), Wannier functions, and strong-coupling perturbation theory. (b) Screening processes excluded/included in the cRPA denoted by P_t/P_r, with t labeling the bands in the target space (i.e., the Ru-t_{2g} bands) and r labeling the rest of the bands (adapted from Ref. [35]).

[39]. The space group $C2/m$ and the structural parameters of α-$RuCl_3$ are taken from neutron diffraction [16]. The DFT with and without spin-orbit coupling is performed in the second variational treatment and the relativistic scalar approximation, respectively [40]. To compute the interaction matrices [defined in Eqs. (13) and (14) below] we include 60 states above the Fermi level and use 2213 LAPW basis functions for the local interactions, and 701 LAPW basis functions for the nonlocal interactions. The calculations of the hopping parameters and the interaction matrices are performed on a $13 \times 13 \times 7$ and a $6 \times 6 \times 4$ k grid, respectively.

The second step is to derive the effective electron-electron interactions using the cRPA [35]. To that end the Hilbert space is divided into two subspaces, the target space t consisting of the bands close to the Fermi level bands and the "rest" space r consisting of all the other bands [see Fig. 1(b)]. Within the cRPA the effective interaction $W_r(x, x', \omega)$ of the states in the target space t screened by the states in the "rest" space r is

$$W_r(x, x', \omega) = \int d^3y \int d^3y' [1 - v(x, y) P_r(y, y', \omega)]^{-1} \times v(y', x'), \tag{1}$$

with $v(x, x')$ the bare Coulomb repulsion and $P_r(x, x', \omega)$ the constrained polarization given by

$$P_r(x, x', \omega) = \sum_{k,j}^{occ} \sum_{k',j'}^{unocc} \left(\frac{\langle k\,j|x\rangle\langle x|k'\,j'\rangle\langle k'\,j'|x'\rangle\langle x'|k\,j\rangle}{\omega - \epsilon_{k'j'} + \epsilon_{kj} + i0^+} - \frac{\langle k'\,j'|x\rangle\langle x|k\,j\rangle\langle k\,j|x'\rangle\langle x'|k'\,j'\rangle}{\omega + \epsilon_{k'j'} - \epsilon_{kj} - i0^+} \right) \tag{2}$$

with ϵ_{kj} and $\langle x|k\,j\rangle$ the Kohn-Sham eigenvalues and eigenfunctions of momentum k and band j obtained from the scalar-relativistic DFT calculation. Unlike the full polarization the constrained polarization in (2) excludes processes taking place within the target space [see Fig. 1(b)]. For the cRPA calculations and the Wannier function transformation described below, the Density Response Code [36] developed for the ELK code is used.

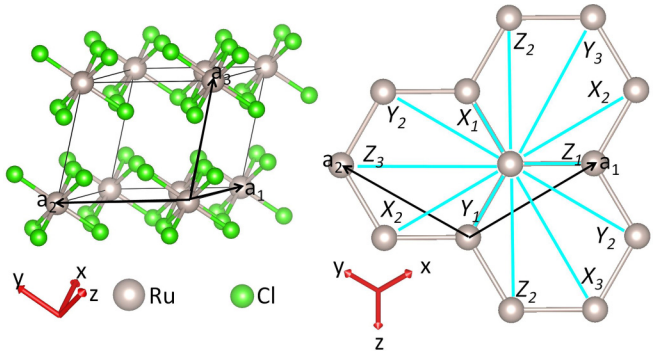

FIG. 2. Definition of the first (X_1, Y_1, Z_1), second (X_2, Y_2, Z_2), and third (X_3, Y_3, Z_3) nearest-neighboring Ru-Ru bonds (cyan lines) and the local coordinates x, y, z (red arrows) relative to the primitive lattice vectors a_1, a_2, a_3 (black arrows) of the $C2/m$ unit cell of α-$RuCl_3$.

The third step is to apply a transformation of the Kohn-Sham eigenfunctions to obtain the generalized multiorbital Hubbard model in the basis of Ru-t_{2g} Wannier functions [41]. Specifically a projected Wannier function transformation [36,42,43] is performed as follows:

$$|rn\rangle = \sum_{kj} e^{ikR(r)} |kj\rangle\langle kj|\phi_n\rangle M_{nn'}(k), \tag{3}$$

where r and n label the atom and orbital indices of the Wannier states, respectively, $R(r)$ labels the unit cell of atom r, $|\phi_n\rangle$ are the projected atomic orbital states, and $M_{nn'}(k)$ is the Löwdin orthogonalization matrix [44] given by

$$M^{-2}_{nn'}(k) = \sum_j \langle\phi_n|kj\rangle\langle kj|\phi_n\rangle, \tag{4}$$

which ensures the Wannier functions are orthonormal. In our study the projected atomic orbitals $|\phi_n\rangle$ are taken to be the Ru-t_{2g} orbitals yz, xz, xy expressed in the local basis defined in Fig. 2 such that the local coordinates (x, y, z) are approximately along the Ru-Cl bonds and the Ru-t_{2g} orbitals satisfy the symmetry properties detailed in Ref. [25]. In the calculations with spin-orbit coupling the spins are rotated into the local coordinate system with the quantization axis along the local z axes. From here we derive the multiorbital generalized t_{2g} Hubbard model. First we define the scalar-relativistic on-site energy and hopping parameters

$$\varepsilon^{sr}_{n_1 n_2} = \sum_{kj} \langle r_1 n_1|kj\rangle \epsilon_{kj} \langle kj|r_1 n_2\rangle, \tag{5}$$

$$t^{sr,r_2-r_1}_{n_1 n_2} = \sum_{kj} \langle r_1 n_1|kj\rangle \epsilon_{kj} \langle kj|r_2 n_2\rangle, \tag{6}$$

with $r_1 \neq r_2$ and ϵ_{kj} and $|kj\rangle$ the Kohn-Sham eigenvalues and eigenstates. Similarly we define on-site energy and hopping parameters from the DFT calculations in which the spin-orbit coupling is included in the second variational treatment:

$$\varepsilon^{vt}_{n_1\sigma_1 n_2\sigma_2} = \sum_{kj} \langle r_1 n_1\sigma_1|kj\rangle \epsilon_{kj} \langle kj|r_1 n_2\sigma_2\rangle, \tag{7}$$

$$t^{vt,r_2-r_1}_{n_1\sigma_1 n_2\sigma_2} = \sum_{kj} \langle r_1 n_1\sigma_1|kj\rangle \epsilon_{kj} \langle kj|r_2 n_2\sigma_2\rangle. \tag{8}$$

From here we define the crystal field Hamiltonian

$$H_{cf} = \sum_r \sum_{n_1,n_2} \sum_\sigma \varepsilon^{sr}_{n_1 n_2} c^\dagger_{rn1\sigma} c_{rn2\sigma} + \text{H.c.}, \tag{9}$$

the hopping Hamiltonian

$$H_{hop} = \sum_{r_1\neq r_2} \sum_{n_1,n_2} \sum_\sigma t^{sr,r_2-r_1}_{n_1 n_2} c^\dagger_{r_1 n_1\sigma} c_{r_2 n_2\sigma} + \text{H.c.}, \tag{10}$$

the local spin-orbit coupling Hamiltonian

$$H^{loc}_{soc} = \sum_r \sum_{n_1,n_2} \sum_{\sigma_1,\sigma_2} \left(\varepsilon^{vt}_{n_1\sigma_1 n_2\sigma_2} - \varepsilon^{sr}_{n_1 n_2}\delta_{\sigma_1\sigma_2}\right) \times \left(c^\dagger_{rn_1\sigma_1} c_{rn_2\sigma_2} + \text{H.c.}\right), \tag{11}$$

and the nonlocal spin-orbit coupling Hamiltonian

$$H^{nloc}_{soc} = \sum_{r_1\neq r_2} \sum_{n_1,n_2} \sum_{\sigma_1,\sigma_2} \left(t^{vt,r_2-r_1}_{n_1\sigma_1 n_2\sigma_2} - t^{sr,r_2-r_1}_{n_1 n_2}\delta_{\sigma_1\sigma_2}\right) \times \left(c^\dagger_{rn_1\sigma_1} c_{rn_2\sigma_2} + \text{H.c.}\right). \tag{12}$$

We restrict the interactions to the local $(r_1 = r_2)$ and nonlocal $(r_1 \neq r_2)$ Hubbard matrices

$$U(r_1 - r_2, n_1, n_2) = \lim_{\omega\to 0} \int d^3x \int d^3x' W(x, x', \omega) \times \langle r_1 n_1|x\rangle\langle x|r_1 n_1\rangle\langle r_2 n_2|x'\rangle\langle x'|r_2 n_2\rangle \tag{13}$$

and the local exchange matrix

$$J(n_1, n_2) = \lim_{\omega\to 0} \int d^3x \int d^3x' W(x, x', \omega) \times \langle rn_1|x\rangle\langle x|rn_2\rangle\langle rn_2|x'\rangle\langle x'|rn_1\rangle. \tag{14}$$

From here we obtain the local interacting Hamiltonian

$$H^{loc}_{int} = U \sum_{rn} n_{rn\uparrow} n_{rn\downarrow} + U' \sum_{r,n\neq n'} n_{rn\uparrow} n_{rn'\downarrow} + J_H \sum_{r,n\neq n'} (c^\dagger_{rn\uparrow} c^\dagger_{rn\downarrow} c_{rn'\downarrow} c_{rn'\uparrow} - c^\dagger_{rn\uparrow} c_{rn\downarrow} c^\dagger_{rn'\downarrow} c_{rn'\uparrow}) + (U' - J) \sum_{r,n<n',\sigma} n_{rn\sigma} n_{rn'\sigma} \tag{15}$$

with U and U' the intra- and interorbital Coulomb repulsion and J_H the Hund's coupling. The nonlocal interacting Hamiltonian is given by

$$H^{nloc}_{int} = \sum_{m=1}^{3} \sum_{\langle r,r'\rangle^m} \sum_{n,n'} \sum_{\sigma,\sigma'} V^m n_{rn\sigma} n_{r'n'\sigma'} \tag{16}$$

with $\langle r, r'\rangle^m$ denoting r and r' being mth-nearest in-plane neighbors and V^m the in-plane mth-nearest-neighboring Coulomb repulsion. The U, U', J_H, and V^m parameters are obtained from orbital-averaging the Hubbard and exchange matrices in Eqs. (13) and (14). After this the multiorbital Hubbard model is assembled:

$$H_{t_{2g}} = H_{cf} + H_{hop} + H^{loc}_{soc} + H^{nloc}_{soc} + H^{loc}_{int} + H^{nloc}_{int}. \tag{17}$$

In the last step, perturbation theory in the strong-coupling limit is performed. To this end the multiorbital Hubbard model

is split into two pieces: the unperturbed part $H_0 = H_{cf} + H_{soc}^{loc} + H_{int}^{loc} + H_{int}^{nloc}$ and the perturbation $\Delta = H_{hop} + H_{soc}^{nloc}$. Then H_0 is diagonalized exactly and Δ is treated with second-order perturbation theory in the strong-coupling limit:

$$\langle l|H_{spin}|l'\rangle = \langle -l|\Delta \sum_h \frac{|h\rangle\langle h|}{E_h - E_l}\Delta|l'\rangle, \tag{18}$$

where $|l\rangle$ and E_l are the degenerate low-energy eigenstates and energies of H_0 that contain 1 hole in each Ru atom and $|h\rangle$ and E_h are all the high-energy eigenstates and energies of H_0 that contain different distributions of the holes.

To simplify the analysis the states $|l\rangle$ are restricted to the lowest-energy Kramers doublet states that are separated from higher-energy states by 165 meV or more. With vanishing crystal field these doublet states reduce to the so-called $j_{\text{eff}} = 1/2$ states [25]. Because of the $SU(2)$ symmetry within the Kramers doublet states, any linear combination between the two Kramers states is also a ground state of H_0 and, therefore, the explicit form of H_{spin} depends on the choice of "gauge." To fix the gauge of these doublet states, we first define up and down pseudospins in the Kramers doublet as being the states that diagonalize $L_z - S_z$. Then, the overall phase is fixed so that the coefficient of $c^\dagger_{r\,yz\uparrow}c^\dagger_{r\,yz\downarrow}c^\dagger_{r\,zx\uparrow}c^\dagger_{r\,zx\downarrow}c^\dagger_{r\,xy-\sigma}|0\rangle$ becomes a real number, where $|0\rangle$ is the vacuum state. We find that this choice of gauge gives more symmetric interactions with respect to the permutation of X, Y, and Z bonds than the one that diagonalizes S_z used in Ref. [10]. We note that the crystal field splits the $j_{\text{eff}} = 3/2$ excited quartet in two Kramers doublets. The gap between the lowest-energy Kramers doublet and the first excited Kramers doublet is 165 meV. The gap between the lowest-energy Kramers doublet and the second excited Kramers doublet is 190 meV. The nonzero matrix elements of $\langle l|H_{spin}|l'\rangle$ are limited to those in which pseudospins on all sites of states $|l\rangle$ and $|l'\rangle$ are the same except for a pair of Ru sites r and r' connected by the perturbation Δ. This allows us to compactly rewrite the spin Hamiltonian in terms of spin operators

$$H_{spin} = \sum_{m=1}^{3} \sum_{\langle rr'\rangle^m} \mathbf{S}_r \cdot \mathbf{J}_{rr'} \cdot \mathbf{S}_{r'} \tag{19}$$

with $\langle r, r'\rangle^m$ denoting r and r' being mth-nearest in-plane neighbors. Other interactions are ignored in this study. Due to the symmetry of the $C2/m$ space group the matrix form of $\mathbf{J}_{rr'}$ is given by

$$\begin{bmatrix} J_m^{xy} + K_m^{xy} & \Gamma_m'^{xy} + \zeta_m & \Gamma_m'^{xy} - \zeta_m \\ \Gamma_m'^{xy} + \zeta_m & J_m^{xy} + \xi_m & \Gamma_m^{xy} \\ \Gamma_m'^{xy} - \zeta_m & \Gamma_m^{xy} & J_m^{xy} - \xi_m \end{bmatrix} \tag{20}$$

for the X_m bond,

$$\begin{bmatrix} J_m^{xy} + \xi_m & \Gamma_m'^{xy} + \zeta_m & \Gamma_m^{xy} \\ \Gamma_m'^{xy} + \zeta_m & J_m^{xy} + K_m^{xy} & \Gamma_m'^{xy} - \zeta_m \\ \Gamma_m^{xy} & \Gamma_m'^{xy} - \zeta_m & J_m^{xy} - \xi_m \end{bmatrix} \tag{21}$$

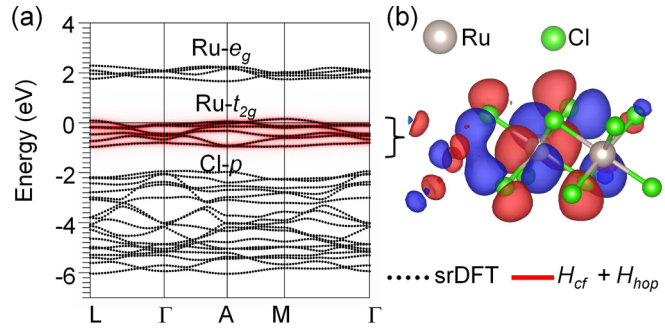

FIG. 3. Left: comparison of the band structure from scalar-relativistic density functional theory (srDFT) and the noninteracting scalar-relativistic part of the Wannier-function-based Hubbard model: $H_{cf} + H_{hop}$. Right: one of the corresponding Ru-t_{2g} Wannier functions.

for the Y_m bond, and

$$\begin{bmatrix} J_m^z & \Gamma_m^z & \Gamma_m'^z \\ \Gamma_m^z & J_m^z & \Gamma_m'^z \\ \Gamma_m'^z & \Gamma_m'^z & J_m^z + K_m^z \end{bmatrix} \tag{22}$$

for the Z_m bond with $m = 1, 2, 3$ in which Dzyaloshinskii-Moriya interactions have been ignored [25].

Finally, to compare with the available experimental studies we consider the following reduced model,

$$H_{spin}^{red} = \sum_{\langle rr'\rangle^1} \left(J_1 \mathbf{S}_r \cdot \mathbf{S}_{r'} + K_1 S_r^\gamma S_{r'}^\gamma + \Gamma_1 S_r^\alpha S_{r'}^\beta + \Gamma_1 S_r^\beta S_{r'}^\alpha\right) + J_3 \sum_{\langle rr'\rangle^3} \left(\mathbf{S}_r \cdot \mathbf{S}_{r'}\right), \tag{23}$$

in which $\{\alpha, \beta, \gamma\}$ is equal to $\{y, z, x\}$, $\{z, x, y\}$, and $\{x, y, z\}$ for the X_1, Y_1, and Z_1 bonds defined in Fig. 2 and in which the first-neighbor Kitaev, Heisenberg, and anisotropy parameters K_1, J_1, and Γ_1 and the third-neighbor Heisenberg parameter J_3 are obtained from bond-averaging the results in Eqs. (19)–(22) and setting the rest of the parameters to zero.

III. RESULTS

In Fig. 3 and Table I we present results corresponding to the noninteracting part of the generalized Hubbard model without spin-orbit coupling, i.e., H_{cf} and H_{hop} defined in Eqs. (9) and (10), respectively. Figure 3(a) shows a comparison of the band structure obtained from scalar-relativistic DFT calculation against the one obtained from the noninteracting

TABLE I. On-site energy and hopping parameters in meV from the noninteracting scalar-relativistic part of the Ru-t_{2g} Wannier-function-based Hubbard model: $H_{cf} + H_{hop}$.

	Local			Z_1 bond			X_1 bond		
	yz	xz	xy	yz	xz	xy	yz	xz	xy
yz	−362	−7	−10	52	160	−21	−98	−16	−12
xz	−7	−362	−10	160	52	−21	−16	46	163
xy	−10	−10	−375	−21	−21	−150	−12	163	47

TABLE II. Elements of the local and nonlocal Hubbard-U matrices and local exchange matrix in meV.

	U local			U Z_1 bond			J local		
	yz	xz	xy	yz	xz	xy	yz	xz	xy
yz	2576	1895	1899	827	893	923		286	288
xz	1895	2576	1899	893	827	923	286		288
xy	1899	1899	2587	923	923	1014	288	288	

scalar-relativistic part of the generalized Hubbard model: $H_{cf} + H_{hop}$. Figure 3(b) shows one of the corresponding Wannier functions that displays a t_{2g} character at the center of the Ru atom and strong Cl-p lobes in the nearest-neighboring Cl atoms. In Table I the local matrix corresponds to H_{cf} on one of the Ru atoms. The hopping matrices correspond to hopping along the Z_1 and X_1 bonds defined in Fig. 2. The crystal field splitting parameters and hopping parameters shown in Table I obey the symmetry properties detailed in Ref. [25]. The hopping parameters corresponding to the second and third nearest-neighboring in-plane Ru-Ru bonds agree with those reported in Ref. [25] within 1 meV.

Table II shows part of the Hubbard and exchange matrices defined in Eqs. (13) and (14). The orbital dependence is relatively weak. Variations are on the order of 10 meV. The orbitally averaged values of the interaction parameters defined in Eq. (15) are given by the intra- and interorbital Coulomb repulsions $U = 2.58$ eV and $U' = 1.9$ eV and the Hund's coupling $J_H = 0.29$ eV. The first, second, and third nearest-neighbor repulsions defined in Eq. (16) are given by $V_1 = 0.9$ eV, $V_2 = 0.53$ eV, and $V_3 = 0.44$ eV, respectively. Our interaction parameters derived for α-$RuCl_3$ closely resemble the values $U = 2.7$ eV, $J_H = 0.28$ eV, and $V_1 = 1.1$ eV obtained from cRPA calculations for another Ru-based compound $SrRu_2O_6$ [45]. We note that in general large nonlocal Coulomb repulsions are expected in realistic models of materials because of the slow decay of the bare Coulomb potential and the fact that screening within the target space should not be included in the derivation of the model parameters to avoid double-counting those effects [35]. For example Hubbard models derived from cRPA for Fe pnictides and chalcogenides [46], ruthenates [45], and iridates [10] all display significant nonlocal Coulomb repulsions relative to their intra-atomic Coulomb repulsions. While the nonlocal Coulomb repulsions have been ignored in many of the previous derivations of the spin models for α-$RuCl_3$ [13,23,25,29,34], they have a significant effect on the magnetic interactions, as we will discuss below.

Table III presents the spin-orbit coupling parameters. Specifically the on-site spin-orbit coupling matrix corresponds to H_{soc}^{loc} defined in Eq. (11). The Z_1 spin-orbit coupling matrix is part of H_{soc}^{nloc} defined in Eq. (12). We note that in previous derivations of the spin Hamiltonian for α-$RuCl_3$ [13,23,25,29,34] a form of the spin-orbit coupling based on atomic orbitals is assumed. Here we investigate how well that assumption compares with the spin-orbit coupling derived with first-principles Wannier functions. The form of the spin-orbit coupling based on atomic t_{2g} orbitals is worked out for

TABLE III. Spin-orbit coupling parameters in meV. Local (middle) and nonlocal (right) parameters derived via first-principles Wannier functions compared to (left) atomic orbital form of the spin-orbit coupling $\frac{\lambda}{2} L \cdot S$ with spin-orbit coupling constant λ fitted to the local part of the spin-orbit coupling derived from first principles.

	Atomic orbital fit $\frac{\lambda}{2} L \cdot S$						Local						Z_1 bond					
	$yz\uparrow$	$xz\uparrow$	$xy\uparrow$	$yz\downarrow$	$xz\downarrow$	$xy\downarrow$	$yz\uparrow$	$xz\uparrow$	$xy\uparrow$	$yz\downarrow$	$xz\downarrow$	$xy\downarrow$	$yz\uparrow$	$xz\uparrow$	$xy\uparrow$	$yz\downarrow$	$xz\downarrow$	$xy\downarrow$
$yz\uparrow$		$59i$	0	0	0	-59		$58i$	i	0	$-1-i$	$-59+i$	0	$1+2i$	0	0	$1+i$	$2+12i$
$xz\uparrow$	$-59i$		0	0	0	$59i$	$-58i$		$-i$	$1+i$	0	$-1+59i$	$1-2i$	0	0	$-1-i$	0	$-12-2i$
$xy\uparrow$	0	0		59	$-59i$	0	$-i$	i		$59-i$	$1-59i$	0	0	0	2	$-2-12i$	$12+2i$	0
$yz\downarrow$	0	0	59		$-59i$	0	0	$1-i$	$59+i$		$-58i$	$-i$	0	$-1+i$	$-2+12i$	0	$1-2i$	0
$xz\downarrow$	0	0	$59i$	$59i$		0	$-1+i$	0	$1+59i$	$58i$		i	$1-i$	0	$12-2i$	$1+2i$	0	0
$xy\downarrow$	-59	$-59i$	0	0	0		$-59-i$	$-1-59i$	0	i	$-i$		$2-12i$	$-12+2i$	0	0	0	2

TABLE IV. Bond-dependent magnetic interaction parameters in meV rounded up to the nearest 0.1 meV for first ($m = 1$), second ($m = 2$), and third ($m = 3$) in-plane nearest-neighboring Ru atoms.

m	J_m^{xy}	J_m^z	K_m^{xy}	K_m^z	Γ_m^{xy}	Γ_m^z	$\Gamma_m'^{xy}$	$\Gamma_m'^z$	ξ_m	ζ_m
1	−0.7	−2.6	−15.3	−14.7	9.1	12.2	−2.2	−2.6	0.2	0.7
2	0.0	0.1	−0.6	−0.8	0.0	0.0	−0.1	−0.1	0.0	0.0
3	0.9	0.9	0.1	0.1	0.0	0.0	−0.1	−0.1	0.0	0.0

example in Ref. [47] and is denoted $\frac{\lambda}{2} L \cdot S$ in Table III. By fitting this form to H_{soc}^{loc} derived from first principles we find the value of the spin-orbit coupling strength to be $\lambda = 118$ meV, which agrees well with the experimentally reported value of 130 meV in Ref. [14]. By comparing the on-site spin-orbit coupling matrix and the atomic orbital fit in Table III we see that the atomic orbital approximation is nearly perfect for the local part of the spin-orbit coupling. However, we also note that there are significant values of the nonlocal spin-orbit coupling that are absent in the atomic orbital approximation for the spin-orbit coupling. Specifically there are large nonlocal spin-orbit couplings between Ru1-xz/yz and Ru2-xy orbitals on the order of 12 meV with Ru1 and Ru2 along the nearest-neighboring Z_1 bond. Similarly sized values of the spin-orbit coupling are found along the X_1 and Y_1 bonds. Along the second and third nearest-neighboring bonds the nonlocal spin-orbit coupling parameters are negligible. The values of the first-neighboring nonlocal spin-orbit coupling parameters of 12 meV are sizable relative to $\frac{\lambda}{2} = 59$ meV given that for each local spin-orbit coupling there are three nearest-neighboring nonlocal spin-orbit couplings on the honeycomb Ru lattice. We note that also in Ref. [10] for the closely related compound Na_2IrO_3 a similar structure of the nonlocal spin-orbit coupling is reported in which the elements between Ir1-xz/yz and Ir2-xy orbitals with Ir1 and Ir2 along the Z_1 bond are significant relative to $\frac{\lambda}{2}$ in that system. The origin of the nonlocal spin-orbit couplings in α-$RuCl_3$ and Na_2IrO_3 and in general any transition metal halide, pnictide, or chalcogenide is the strong hybridization between the transition metal d orbitals and the anion p orbitals exemplified by the Wannier function shown in Fig. 3(b). An interesting question is what the influence of such nonlocal spin-orbit coupling parameters will be on the magnetic exchanges in α-$RuCl_3$.

Having obtained the first-principles generalized Hubbard model we next perform the strong-coupling perturbation theory detailed in Eqs. (19)–(22) to derive the magnetic interactions shown in Table IV. Just as in, for example, Ref. [25], we find that some of the parameters display sizable variations depending on the bond directions. This illustrates the complex dependence of the magnetic interactions on the details of the crystal structure and the need for their derivation from first principles.

Nonetheless we proceed by deriving the parameters of the simplified bond-averaged model defined in Eq. (23) to be able to compare to the available experimental studies. The results are listed in Table V. Specifically, we consider three cases. Case 1 corresponds to the full first-principles model. Cases 2 and 3 correspond to the first-principles model in which the nonlocal interactions and spin-orbit coupling are omitted, respectively. When we compare case 1 with case 2 we note that the effect of the nonlocal interactions is to significantly increase the nearest-neighbor magnetic interactions roughly by a factor 3–7. To understand this we consider in Fig. 4 a low- and a high-energy state in a simple model consisting of 6 sites with 1 orbital per site, nearest-neighbor hopping t, and local and nonlocal Coulomb repulsions U and V, respectively. By counting nearest-neighboring holes in both cases (indicated with cyan lines in Fig. 4) we see that the corresponding energies are $E_l = 5V$ for the low-energy state and $E_h = U + 4V$ for the high-energy state. When we plug these values into Eq. (18) we see that the magnetic interactions go as $t^2/(U - V)$ instead of the usual t^2/U. In other words the effect of the nonlocal repulsions will be to enhance the magnetic interactions. These enhancements are quite strong given the large size of the nearest-neighbor nonlocal interaction $V_1 = 0.9$ eV compared to the intra-atomic repulsion $U = 2.58$ eV. From comparing cases 1 and 3 we note that the effect of the nonlocal spin-orbit coupling is not as dramatic as that of the nonlocal interactions. Still its influence is non-negligible for the first-neighbor Kitaev (K_1), increasing it by about 14%.

TABLE V. Bond-averaged magnetic interaction parameters in meV derived for three different cases compared to experimental reports [20–22,26,28,30–33] with $C = 3J_1 + K_1$. The parameters deduced from magnetic-specific-heat data [26] have been bond averaged.

	J_1	K_1	Γ_1	J_3	C
This study case 1 full	−1.3	−15.1	10.1	0.9	−19.1
This study case 2 w/o H_{int}^{nloc}	−0.2	−4.8	3.1	0.7	−5.3
This study case 3 w/o H_{soc}^{nloc}	−1.3	−13.3	9.4	1.0	−17.3
Inelastic neutron scat. [28]	0	−6.8	9.5	0	−6.8
Inelastic neutron scat. [20]	−0.5	−5	2.5	0.5	−6.5
Thermal Hall effect [32,33]	−0.5	−5	2.5	0.1125	−6.5
THz spectroscopy [21]	−0.35	−2.8	2.4	0.34	−3.9
Anisotropic susceptibility [22]	n.a.	n.a.	29.2	n.a.	16.9
Mag. specific heat [26,30,31]	−1.5	−24.4	5.3	0	−29.0

IV. DISCUSSION

From Table V we see that the parameters derived in our fully first-principles study differ significantly compared to the values of previous experimental fits. Why this is the case remains an open question. First of all, it is important to note that

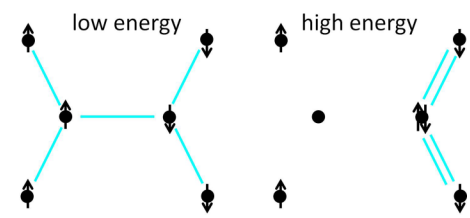

FIG. 4. Comparison of low- and high-energy states in simplified model with 1 orbital per site. Arrows indicate spin-up and spin-down holes and cyan lines indicate nearest-neighboring holes.

there are significant variations in the experimentally derived parameters. For example the Kitaev coupling K_1 derived from THz spectroscopy and magnetic specific heat differ by more than a factor 5. Given this, it is possible that the disagreement between our theoretical results and the experiments reflects difficulties in deducing the parameters from the experiments. Here we will not discuss possible issues on the experimental side and focus on potential problems in the first-principles derivation instead. The derivation of the magnetic parameters in this study is based on unbiased first-principles calculations. Nonetheless, approximations are made in the derivation of the low-energy electronic Hamiltonian ($H_{t_{2g}}$) and the strong-coupling perturbation theory.

In the strong-coupling limit the effects of interactions and spin-orbit coupling form the starting point of the analysis and the hopping parameters are treated as a perturbation. The opposite limit, however, has also been considered for Na_2IrO_3 [11] and α-$RuCl_3$ [16], in which the strong anion p assisted hopping between transition metal t_{2g} orbitals leads to the formation of quasimolecular orbitals on the Ru hexagons similar to the molecular orbitals in benzene. Moreover, in Ref. [25] it was concluded that the strong-coupling perturbation theory for α-$RuCl_3$ and A_2IrO_3 with $A = $ Na, Li does not converge and that instead exact diagonalization is needed to derive the magnetic interactions from the Hubbard model. This conclusion was reached even without taking into account the nonlocal interactions that push α-$RuCl_3$ farther away from the strong-coupling limit. If indeed α-$RuCl_3$ not being in the strong-coupling limit is the reason for the large mismatch between the experimental fits and our theoretical results, this would be an important point given that many of the theoretical derivations for α-$RuCl_3$ or quantum spin-liquid materials in general are based on this approximation. It should be noted that in Ref. [10] the exact same procedure was followed as in this paper to derive the spin model for Na_2IrO_3 that was found to agree well with experiments. Given that the Ir-5d orbitals are more delocalized compared to the Ru-4d orbitals one would expect that α-$RuCl_3$ is closer to the strong-coupling limit than Na_2IrO_3. One interesting possibility would be to apply the exact-diagonalization procedure of Ref. [25] to the Hubbard model in this work.

A second approximation made in our derivation is the cRPA. There have been recent reports that the cRPA tends to overscreen the interactions [48–50]. An underestimate of the strength of screened Coulomb repulsions via cRPA would lead to an overestimate of the magnetic exchange couplings. We note that two of these studies [48,49] are based on simple models that possibly could exaggerate the overscreening effects in cRPA compared to cases with realistic electronic structures. In Ref. [50], on the other hand, the target bands are entangled with the rest of the bands, which could also cause discrepancies between different methods unrelated to overscreening.

In addition to the potential problem of overscreening, there is the issue that the effects of the Coulomb repulsion are double counted. At the level of DFT the effect of interactions within the target space are already included via the Hartree and exchange correlation functionals in addition to their treatment in the strong-coupling perturbation theory. Furthermore, in our derivation of the magnetic exchange coupling we ignored the frequency dependence of the interaction parameters [cf. Eqs. (13) and (14)]. A constrained GW approximation has been proposed to remedy the double-counting issue and to renormalize the frequency dependence of the interaction parameters into static ones [51,52].

TABLE VI. Bond-dependent magnetic interaction parameters for case 2, neglecting nonlocal interactions. The parameters are given in meV rounded up to the nearest 0.1 meV for first ($m = 1$), second ($m = 2$), and third ($m = 3$) in-plane nearest-neighboring Ru atoms.

m	J_m^{xy}	J_m^{z}	K_m^{xy}	K_m^{z}	Γ_m^{xy}	Γ_m^{z}	$\Gamma_m'^{xy}$	$\Gamma_m'^{z}$	ξ_m	ζ_m
1	−0.1	−0.5	−4.6	−4.5	2.7	3.6	−0.7	−0.8	−0.1	0.2
2	0.0	0.0	−0.3	−0.4	0.0	0.0	0.0	0.0	0.0	0.0
3	0.8	0.7	0.1	0.1	0.0	0.0	0.0	0.0	0.1	0.0

We would like to point out that in Table V there is a relatively good agreement between the model derived without the nonlocal interactions (case 2) and the fitted parameters obtained from one of the inelastic-neutron-scattering experiments [25]. Therefore it might be tempting to ignore the nonlocal interactions. However, given that there is no justification as to why nonlocal interactions could be ignored, we regard this as a coincidence with no physical meaning.

Another approximation made in our derivation of the magnetic exchange couplings is the orbital averaging of the interaction matrices. This could influence the magnetic interactions, especially given the relatively strong orbital dependence of the nonlocal interaction matrices (see for example the interaction matrix along the Z_1 bond in Table II). The orbitally symmetric nonlocal interaction Hamiltonian H_{int}^{nloc} is diagonal in the eigenbasis of the local part of the Hamiltonian: $H_{cf} + H_{soc}^{loc} + H_{int}^{loc}$. This is why we could treat the nonlocal interaction as part of the unperturbed part of the Hamiltonian. For an orbitally nonsymmetric nonlocal Hamiltonian this no longer works. In principle, it could be possible to treat the orbitally nonsymmetric nonlocal Hamiltonian as part of the perturbation. Such a treatment will be left to explore in future studies.

Finally we note that our model, as most other models in the literature, does not include the out-of-plane magnetic exchange couplings. The reason is that the interlayer structure of α-$RuCl_3$ has been difficult to resolve experimentally. Various interlayer structures have been reported including the trigonal space group $P3_112$, the rhombohedral space group $R\bar{3}$, and the monoclinic space group $C2/m$ with AB and ABC stackings [14,16,17,53]. The difficulty in determining the out-of-plane structure most likely stems from the weak van

TABLE VII. Bond-dependent magnetic interaction parameters for case 3, neglecting nonlocal spin-orbit coupling. The parameters are given in meV rounded up to the nearest 0.1 meV for first ($m = 1$), second ($m = 2$), and third ($m = 3$) in-plane nearest-neighboring Ru atoms.

m	J_m^{xy}	J_m^{z}	K_m^{xy}	K_m^{z}	Γ_m^{xy}	Γ_m^{z}	$\Gamma_m'^{xy}$	$\Gamma_m'^{z}$	ξ_m	ζ_m
1	−0.7	−2.6	−13.3	−13.2	8.4	11.3	−2.2	−2.5	0.6	0.7
2	0.0	0.0	−0.6	−0.8	0.0	0.0	0.0	0.0	0.0	0.0
3	1.0	0.9	0.1	0.1	0.0	0.0	0.0	0.0	0.0	0.0

der Waals bonding between the $RuCl_3$ layers that allows the layers to easily slide over one another. Related to this, stacking faults have been reported to be present in α-$RuCl_3$, which also adds to the difficulty of resolving the out-of-plane structure [14,16,17].

Our finding contributes to the understanding and design of quantum spin-liquid materials. Per definition, first-principles models have no free parameters and can thus help constrain the multitude of models that have been proposed for α-$RuCl_3$ in the literature [20–29]. Furthermore, first-principles calculations describe the complexity of the full spin model and its dependence on subtle structural distortions without neglecting or bond-averaging the parameters. Ultimately, an accurate first-principles method will allow not only for the understanding of the current quantum spin-liquid candidate materials but also for predicting how their properties can be optimized by pressure, chemical doping, and heterostructure engineering or how to design new quantum spin-liquid materials virtually via high-throughput computations. Laying out potential problems of the theoretical approaches used in this study for the case of α-$RuCl_3$ will motivate the search for improved first-principles techniques in future efforts to derive first-principles models for quantum spin-liquid materials.

V. CONCLUSION

We have derived the magnetic exchange couplings of α-$RuCl_3$ via first-principles techniques. To this end we utilized the constrained random phase approximation (cRPA) to derive the Ru-t_{2g} Wannier-function-based generalized Hubbard model to which we applied second-order perturbation theory in the limit of the hopping parameters being small compared to the interactions. We have found that the first, second, and third nearest-neighboring Coulomb repulsions are significant compared to the on-site ones. Furthermore, we found sizable elements in the spin-orbit coupling between orbitals on nearest-neighboring Ru atoms that are usually ignored in model treatments of the spin-orbit coupling based on atomic orbitals instead of realistic first-principles Wannier functions. We have investigated the effect of both the nonlocal interaction and the nonlocal spin-orbit coupling on the magnetic exchange couplings. The nonlocal interactions are found to strongly enhance the magnetic exchange couplings. The nonlocal spin-orbit coupling overall has a less dramatic effect although it still has a sizable influence on the Kitaev interaction strength. Our full model that includes the influence of both local and nonlocal interactions and spin-orbit coupling has magnetic exchange couplings that differ from the ones obtained thus far from experimental fits. Highlighting the importance of nonlocal electron-electron interaction and spin-orbit coupling effects and laying out potential problems in the combined cRPA, Wannier function, and strong-coupling theory approach in our study contributes to the understanding and virtual engineering of quantum spin-liquid candidate materials via first-principles calculations.

The DOE will provide public access to these results of federally sponsored research in accordance with the DOE Public Access Plan [54].

ACKNOWLEDGMENTS

We thank A. Banerjee, S. E. Nagler, G. J. Halász, D. A. Tennant, A. M. Samarakoon, R. Valentí, S. M. Winter, and D. Mandrus for valuable suggestions and discussions. P.L., S.O., and T.B. acknowledge support from the Scientific Discovery through Advanced Computing (SciDAC) program funded by the US Department of Energy, Office of Science, Advanced Scientific Computing Research and Basic Energy Sciences, Division of Materials Sciences and Engineering. A portion of the work was conducted at the Center for Nanophase Materials Sciences, which is a DOE Office of Science User Facility. DD-OLCF (ORNL) Award "MAT160" of Titan supercomputer time is acknowledged with thanks (A.G.E.).

This manuscript has been authored by UT-Battelle, LLC, under Contract DE-AC05-00OR22725 with the U.S. Department of Energy (DOE). The U.S. government retains and the publisher, by accepting the article for publication, acknowledges that the US government retains a nonexclusive, paid-up, irrevocable, worldwide license to publish or reproduce the published form of this manuscript, or allow others to do so, for US government purposes.

APPENDIX: FULL BOND-DEPENDENT PARAMETERS FOR CASE 2 AND CASE 3

The bond-dependent interactions for the full *ab initio* model were given in Table IV. Table V also lists bond-averaged parameters for the case of neglected nonlocal interactions (case 2) and nonlocal spin-orbit coupling (case 3). For completeness, the full bond-dependent magnetic interaction parameters for these cases are shown in Table VI and Table VII, respectively.

[1] A. Kitaev, Ann. Phys. **321**, 2 (2006).
[2] A. Kitaev, Ann. Phys. **303**, 2 (2003).
[3] C. Nayak, S. H. Simon, A. Stern, M. Freedman, and S. Das Sarma, Rev. Mod. Phys. **80**, 1083 (2008).
[4] G. Jackeli and G. Khaliullin, Phys. Rev. Lett. **102**, 017205 (2009).
[5] J. Chaloupka, G. Jackeli, and G. Khaliullin, Phys. Rev. Lett. **105**, 027204 (2010).
[6] X. Liu, T. Berlijn, W.-G. Yin, W. Ku, A. Tsvelik, Y.-J. Kim, H. Gretarsson, Y. Singh, P. Gegenwart, and J. P. Hill, Phys. Rev. B **83**, 220403(R) (2011).
[7] S. K. Choi, R. Coldea, A. N. Kolmogorov, T. Lancaster, I. I. Mazin, S. J. Blundell, P. G. Radaelli, Y. Singh, P. Gegenwart, K. R. Choi *et al.*, Phys. Rev. Lett. **108**, 127204 (2012).
[8] F. Ye, S. Chi, H. Cao, B. C. Chakoumakos, J. A. Fernandez-Baca, R. Custelcean, T. F. Qi, O. B. Korneta, and G. Cao, Phys. Rev. B **85**, 180403(R) (2012).
[9] I. Kimchi and Y.-Z. You, Phys. Rev. B **84**, 180407(R) (2011).
[10] Y. Yamaji, Y. Nomura, M. Kurita, R. Arita, and M. Imada, Phys. Rev. Lett. **113**, 107201 (2014).
[11] I. I. Mazin, H. O. Jeschke, K. Foyevtsova, R. Valentí, and D. I. Khomskii, Phys. Rev. Lett. **109**, 197201 (2012).

[12] K. W. Plumb, J. P. Clancy, L. J. Sandilands, V. V. Shankar, Y. F. Hu, K. S. Burch, H.-Y. Kee, and Y.-J. Kim, Phys. Rev. B **90**, 041112(R) (2014).

[13] H.-S. Kim, V. Shankar V., A. Catuneanu, and H.-Y. Kee, Phys. Rev. B **91**, 241110(R) (2015).

[14] A. Banerjee, C. A. Bridges, J.-Q. Yan, A. A. Aczel, L. Li, M. B. Stone, G. E. Granroth, M. D. Lumsden, Y. Yiu, J. Knolle *et al.*, Nat. Mater. **15**, 733 (2016).

[15] J. A. Sears, M. Songvilay, K. W. Plumb, J. P. Clancy, Y. Qiu, Y. Zhao, D. Parshall, and Y.-J. Kim, Phys. Rev. B **91**, 144420 (2015).

[16] R. D. Johnson, S. C. Williams, A. A. Haghighirad, J. Singleton, V. Zapf, P. Manuel, I. I. Mazin, Y. Li, H. O. Jeschke, R. Valentí *et al.*, Phys. Rev. B **92**, 235119 (2015).

[17] H. B. Cao, A. Banerjee, J.-Q. Yan, C. A. Bridges, M. D. Lumsden, D. G. Mandrus, D. A. Tennant, B. C. Chakoumakos, and S. E. Nagler, Phys. Rev. B **93**, 134423 (2016).

[18] A. Banerjee, P. Lampen-Kelley, J. Knolle, C. Balz, A. A. Aczel, B. Winn, Y. Liu, D. Pajerowski, J. Yan, C. A. Bridges *et al.*, npj Quantum Mater. **3**, 8 (2018).

[19] Y. Kasahara, T. Ohnishi, Y. Mizukami, O. Tanaka, S. Ma, K. Sugii, N. Kurita, H. Tanaka, J. Nasu, Y. Motome *et al.*, Nature (London) **559**, 227 (2018).

[20] S. M. Winter, K. Riedl, P. A. Maksimov, A. L. Chernyshev, A. Honecker, and R. Valentí, Nat. Commun. **8**, 1152 (2017).

[21] L. Wu, A. Little, E. E. Aldape, D. Rees, E. Thewalt, P. Lampen-Kelley, A. Banerjee, C. A. Bridges, J.-Q. Yan, D. Boone *et al.*, Phys. Rev. B **98**, 094425 (2018).

[22] P. Lampen-Kelley, S. Rachel, J. Reuther, J.-Q. Yan, A. Banerjee, C. A. Bridges, H. B. Cao, S. E. Nagler, and D. Mandrus, Phys. Rev. B **98**, 100403(R) (2018).

[23] H.-S. Kim and H.-Y. Kee, Phys. Rev. B **93**, 155143 (2016).

[24] R. Yadav, N. A. Bogdanov, V. M. Katukuri, S. Nishimoto, J. van den Brink, and L. Hozoi, Sci. Rep. **6**, 37925 (2016).

[25] S. M. Winter, Y. Li, H. O. Jeschke, and R. Valentí, Phys. Rev. B **93**, 214431 (2016).

[26] T. Suzuki and S.-i. Suga, Phys. Rev. B **97**, 134424 (2018).

[27] S. M. Winter, A. A. Tsirlin, M. Daghofer, J. van den Brink, Y. Singh, P. Gegenwart, and R. Valentí, J. Phys.: Condens. Matter **29**, 493002 (2017).

[28] K. Ran, J. Wang, W. Wang, Z. Y. Dong, X. Ren, S. Bao, S. Li, Z. Ma, Y. Gan, Y. Zhang, J. T. Park, G. Deng, S. Danilkin, S. L. Yu, J. X. Li, and J. Wen, Phys. Rev. Lett. **118**, 107203 (2017).

[29] W. Wang, Z.-Y. Dong, S.-L. Yu, and J.-X. Li, Phys. Rev. B **96**, 115103 (2017).

[30] Y. Kubota, H. Tanaka, T. Ono, Y. Narumi, and K. Kindo, Phys. Rev. B **91**, 094422 (2015).

[31] S.-H. Do, S.-Y. Park, J. Yoshitake, J. Nasu, Y. Motome, Y. Kwon, D. T. Adroja, D. J. Voneshen, K. Kim, T.-H. Jang *et al.*, Nat. Phys. **13**, 1079 (2017).

[32] J. Cookmeyer and J. E. Moore, Phys. Rev. B **98**, 060412(R) (2018).

[33] Y. Kasahara, K. Sugii, T. Ohnishi, M. Shimozawa, M. Yamashita, N. Kurita, H. Tanaka, J. Nasu, Y. Motome, T. Shibauchi *et al.*, Phys. Rev. Lett. **120**, 217205 (2018).

[34] Y. S. Hou, H. J. Xiang, and X. G. Gong, Phys. Rev. B **96**, 054410 (2017).

[35] F. Aryasetiawan, T. Miyake, and R. Sakuma, in *The LDA+DMFT Approach to Strongly Correlated Materials*, edited by E. Pavarini, E. Koch, D. Vollhardt, and A. Lichtenstein (Forschungszentrum Jülich GmbH Institute for Advanced Simulations, Jülich, 2004), Chap. 7.

[36] A. Kozhevnikov, A. G. Eguiluz, and T. C. Schulthess, in *SC '10: Proceedings of the 2010 ACM/IEEE International Conference for High Performance Computing, Networking, Storage and Analysis* (IEEE Computer Society, Washington, DC, 2010), pp. 1–10.

[37] R. Arita, J. Kuneš, A. V. Kozhevnikov, A. G. Eguiluz, and M. Imada, Phys. Rev. Lett. **108**, 086403 (2012).

[38] J. P. Perdew, K. Burke, and M. Ernzerhof, Phys. Rev. Lett. **77**, 3865 (1996).

[39] See http://elk.sourceforge.net.

[40] D. J. Singh and L. Nordstrom, *Planewaves, Pseudopotentials, and the LAPW Method* (Springer, Berlin, 2006).

[41] N. Marzari and D. Vanderbilt, Phys. Rev. B **56**, 12847 (1997).

[42] W. Ku, H. Rosner, W. E. Pickett, and R. T. Scalettar, Phys. Rev. Lett. **89**, 167204 (2002).

[43] V. I. Anisimov, D. E. Kondakov, A. V. Kozhevnikov, I. A. Nekrasov, Z. V. Pchelkina, J. W. Allen, S.-K. Mo, H.-D. Kim, P. Metcalf, S. Suga *et al.*, Phys. Rev. B **71**, 125119 (2005).

[44] I. Mayer, Int. J. Quantum Chem. **90**, 63 (2002).

[45] W. Tian, C. Svoboda, M. Ochi, M. Matsuda, H. B. Cao, J.-G. Cheng, B. C. Sales, D. G. Mandrus, R. Arita, N. Trivedi, and J. Q. Yan, Phys. Rev. B **92**, 100404(R) (2015).

[46] T. Miyake, K. Nakamura, R. Arita, and M. Imada, J. Phys. Soc. Jpn. **79**, 044705 (2010).

[47] M. D. Jones and R. C. Albers, Phys. Rev. B **79**, 045107 (2009).

[48] C. Honerkamp, H. Shinaoka, F. F. Assaad, and P. Werner, Phys. Rev. B **98**, 235151 (2018).

[49] Q. Han, B. Chakrabarti, and K. Haule, arXiv:1810.06116.

[50] T. Tadano, Y. Nomura, and M. Imada, Phys. Rev. B **99**, 155148 (2019).

[51] M. Hirayama, T. Miyake, and M. Imada, Phys. Rev. B **87**, 195144 (2013).

[52] M. Hirayama, T. Misawa, T. Ohgoe, Y. Yamaji, and M. Imada, Phys. Rev. B **99**, 245155 (2019).

[53] S.-Y. Park, S.-H. Do, K.-Y. Choi, D. Jang, T.-H. Jang, J. Schefer, C.-M. Wu, J. S. Gardner, J. M. S. Park, and S. Ji, arXiv:1609.05690.

[54] http://energy.gov/downloads/doe-public-access-plan.